

Focal mechanisms and the stress field in the aftershock area of the 2018 Hokkaido Eastern Iburi earthquake ($M_{JMA} = 6.7$)

Yuki Susukida

Hokkaido Daigaku Rigakubu Daigakuin Rigaku Kenkyuka Rigakuin

Kei Katsumata (✉ kkatsu@sci.hokudai.ac.jp)

Hokkaido <https://orcid.org/0000-0001-9727-4515>

Masayoshi Ichiyanagi

Hokkaido Daigaku Rigakubu Daigakuin Rigaku Kenkyuka Rigakuin

Mako Ohzono

Hokkaido Daigaku Rigakubu Daigakuin Rigaku Kenkyuka Rigakuin

Hiroshi Aoyama

Hokkaido Daigaku Rigakubu Daigakuin Rigaku Kenkyuka Rigakuin

Ryo Tanaka

Hokkaido Daigaku Rigakubu Daigakuin Rigaku Kenkyuka Rigakuin

Masamitsu Takada

Hokkaido Daigaku Rigakubu Daigakuin Rigaku Kenkyuka Rigakuin

Teruhiro Yamaguchi

Hokkaido Daigaku Rigakubu Daigakuin Rigaku Kenkyuka Rigakuin

Kazumi Okada

Hokkaido Daigaku Rigakubu Daigakuin Rigaku Kenkyuka Rigakuin

Hiroaki Takahashi

Hokkaido Daigaku Rigakubu Daigakuin Rigaku Kenkyuka Rigakuin

Shin'ichi Sakai

Tsukuba Daigaku - Tokyo Campus Bunkyo Kosha

Satoshi Matsumoto

Kyushu Daigaku

Tomomi Okada

Tohoku Daigaku - Aobayama Shin Campus

Toru Matsuzawa

Tohoku Daigaku - Aobayama Shin Campus

Hiroki Miyamachi

Kagoshima Daigaku

Shuichiro Hirano

Kagoshima Daigaku

Yoshiko Yamanaka

Nagoya Daigaku

Shinichiro Horikawa

Nagoya Daigaku

Masahiro Kosuga

Hirosaki Daigaku

Hiroshi Katao

Kyoto Daigaku

Yoshihisa Iio

Kyoto Daigaku

Airi Nagaoka

Kyoto Daigaku

Noriko Tsumura

Chiba Daigaku

Tomotaka Ueno

National Research Institute for Earth Science and Disaster Resilience

the Group for the Aftershock Observations of the 2018 Hokkaido Eastern Iwate Earthquake

Hokkaido Daigaku Rigakubu Daigakuin Rigaku Kenkyuka Rigakuin

Full paper

Keywords: the Hokkaido Eastern Iwate earthquake, reverse fault, aftershock distribution, focal mechanism solution, temporary seismic network, stress inversion

Posted Date: September 22nd, 2020

DOI: <https://doi.org/10.21203/rs.3.rs-41024/v2>

License:  This work is licensed under a Creative Commons Attribution 4.0 International License.

[Read Full License](#)

Version of Record: A version of this preprint was published at Earth, Planets and Space on January 1st, 2021. See the published version at <https://doi.org/10.1186/s40623-020-01323-x>.

Abstract

The tectonic stress field was investigated in and around the aftershock area of the Hokkaido Eastern Iburi earthquake ($M_{JMA} = 6.7$) occurred on 6 September 2018. We deployed 26 temporary seismic stations in the aftershock area for approximately 2 months and located 1785 aftershocks precisely. Among these aftershocks 818 focal mechanism solutions were determined using the first motion polarity of P wave from the temporary observation and the permanent seismic networks of Hokkaido University, Japan Meteorological Agency (JMA), and High Sensitivity Seismograph Network Japan (Hi-net). We found that (1) the reverse faulting and the strike-slip faulting are dominant in the aftershock area, (2) the average trend of P- and T-axes are $78^\circ \pm 33^\circ$ and $357^\circ \pm 52^\circ$, respectively, and (3) the average plunge of P- and T-axes are $25^\circ \pm 16^\circ$ and $46^\circ \pm 20^\circ$, respectively: the P-axis is close to be horizontal and the T-axis is more vertical than the average of the P-axes. We applied a stress inversion method to the focal mechanism solutions to estimate a stress field in the aftershock area. As a result, we found that the reverse fault type stress field is dominant in the aftershock area. An axis of the maximum principal stress (σ_1) has the trend of $73^\circ \pm 8^\circ$ and the dipping eastward of $17^\circ \pm 6^\circ$ and an axis of the intermediate principal stress (σ_2) has the trend of $126^\circ \pm 91^\circ$ and the dipping southward of $16^\circ \pm 13^\circ$, indicating that both of σ_1 - and σ_2 -axes are close to be horizontal. An axis of the minimum principal stress (σ_3) has the dipping westward of $64^\circ \pm 9^\circ$ that is close to be vertical. The results strongly suggest that the reverse-fault-type stress field is predominant as an average over the aftershock area which is in the western boundary of the Hidaka Collision Zone. The average of the stress ratio $R = (\sigma_1 - \sigma_2) / (\sigma_1 - \sigma_3)$ is 0.6 ± 0.2 in the whole aftershock area. Although not statistically significant, we suggested that R decreases systematically as the depth is getting deep, which is modeled by a quadratic polynomial of depth.

Introduction

The tectonic regime is complicated in Hokkaido corner, Japan subduction zone (Fig. 1). The Pacific (PA) plate is moving toward $N63^\circ W$ with a speed of 8.2 cm/y (DeMets et al 1994) and subducting below the North American (NA) plate or the Okhotsk (OK) plate on which the Hokkaido Island is located (Takahashi et al 1999; Katsumata et al 2002,2003). The upper surface of the PA plate strongly coupled with the overriding plate in and around the Kurile Trench (Hashimoto et al 2009) and shallow great earthquakes have been caused repeatedly. This subduction process possibly produces a compressional stress field with the direction of NW-SE in the inland area of Hokkaido Island. Moreover, a collision process is in progress. The Kurile Islands arc and the NE Japan arc are colliding in and around the Hidaka Mountain Range (HMR) (Kimura 1981,1986,1996; Seno 1985; Moriya 1986; Arita et al 2001). This is called the Hidaka Collision Zone (HCZ). The speed of the collision is estimated to be 6-11 mm/y relative to the NA plate based on the horizontal slip direction from shallow-thrust earthquakes (DeMets 1992). This collision process possibly produces a compressional stress field in the HCZ with the direction of NE-SW. Additionally, the upper crust and the lower crust beneath the HCZ are not a simple layered structure (Ozel et al 1996; Moriya et al 1998; Iwasaki et al 2004; Shiina et al 2018).

Some tectonic models have been proposed for the HCZ. The crust of the Kurile Islands arc has been torn in the east of the HMR due to the collision and divided into the upper part and the lower part (Ito et al 1999; Murai et al 2003). The upper part is riding over the NE Japan arc in the west of the HMR. The lower part is in contact with the upper boundary of the PA plate, dragged into the upper mantle and scraped (Moriya 1999; Tsumura et al 1999). Kita et al (2012) insisted that the mantle material might be rising directly from the uppermost mantle of the Kurile Islands arc. These complicated structures may cause a complicated stress field and produce earthquakes with a variety of the focal mechanisms.

Recently, two large earthquakes occurred in the crust of the HCZ: the 1970 Hidaka earthquake ($M_{JMA} = 6.7$) (Motoya and Kitagamae 1971; Moriya 1972) and the 1982 Urakawa-oki earthquake ($M_{JMA} = 7.1$) (Moriya et al 1983). The focal mechanism solutions of the two earthquakes are similar: the reverse faulting with the P-axis in the direction of NE-SW (Kita et al 2012). Both two earthquakes were in the central part of the HCZ and thus the compressional stress filed in the direction of NE-SW is dominant at least in the central part of the HCZ. This idea was supported by Terakawa and Matsu'ura (2010), founding that the reverse-fault-type stress field is dominant in and around the HCZ and the maximum principal stress (σ_1) is oriented to nearly NE-SW. Kita et al (2012) applied a stress inversion analysis to small earthquakes in the central part of the HCZ and they found that the σ_1 -axis is oriented to nearly NE-SW.

In the western boundary of the HCZ, a large earthquake occurred on 6 September 2018: The Hokkaido Eastern Iburi earthquake ($M_{JMA} = 6.7$). Although the focal mechanism of the main shock was estimated as a strike-slip faulting by using the first motion polarities of P wave (JMA 2018b; NIED 2018b; Katsumata et al 2019), the centroid moment tensor (CMT) solution shows the reverse faulting with the P-axis in the direction of NE-SW (JMA 2018a; NIED 2018a). The mismatch between the focal mechanism solution and the CMT solution has been explained by a model that a large reverse faulting occurred immediately after an initial rupture of a small strike-slip faulting (Katsumata et al 2019). The CMT solution of the 2018 Hokkaido Eastern Iburi earthquake is similar to the focal mechanisms of the 1970 Hidaka earthquake and the 1982 Urakawa-oki earthquake, clearly indicating that the compressional stress field due to the collision extends to the western boundary of the HCZ (Terakawa and Matsu'ura 2010; Hua et al 2019).

The main shock of the 2018 Hokkaido Eastern Iburi earthquake was followed by many aftershocks. We deployed temporary seismic stations densely in the aftershock area to determine the hypocenters and the focal mechanisms accurately. The purpose of this study is to determine the focal mechanisms of the aftershocks, to apply a stress inversion method to the focal mechanisms, and to make some discussions on the detailed spatial pattern of the stress field in the aftershock area.

Data

To obtain aftershocks data in detail, we deployed 26 temporary seismic stations in the focal area immediately after the main shock and observed aftershocks for approximately 2 months (Fig. 2 and Additional file 1). The temporary observation was conducted by the Group for the Aftershock Observations of the 2018 Hokkaido Eastern Iwate Earthquake, which consists of Hokkaido University, Hirosaki University, Tohoku University, Chiba University, the University of Tokyo, Nagoya University, Kyoto University, Kyushu University, Kagoshima University, and the National Research Institute for Earth Science and Disaster Resilience (NIED). The temporary seismographic stations consisted of 4 telemetered systems and 22 portable offline systems. We also used 183 permanent online seismographic stations maintained by Hokkaido University, JMA, and NIED. Waveform data observed during the period from 6 September 2018 to 31 October 2018 were examined carefully by visual inspection, and the arrival times of P and S waves and the first motion polarities of P wave were read manually by a well-trained person.

Methods

We determined hypocenters of earthquakes with the maximum likelihood estimation algorithm of Hirata and Matsu'ura (1987) using the 1D velocity structure of P wave based on Kasahara et al (1994) (Fig. 2), which is the same as that used for the hypocenter calculation at the Hokkaido University. The S wave velocity was obtained by the relationship $V_S = V_P / 1.7$, where V_P and V_S are the P and S wave velocities, respectively. We located 1785 earthquakes in the study area (42.5-42.9°N, 141.8-142.2°E), observed from 2018-09-06 03:00 to 2018-10-31 23:59 with depths shallower than 50 km and the magnitude ranging from 0.2 to 5.9 (Fig. 3).

We determined focal mechanism solutions of earthquakes by using a grid-search technique developed by Hardebeck and Shearer (2002). We used two 1D velocity structures to take the uncertainty of ray paths, especially take-off angle from the hypocenter, into account (Fig. 2). The first one is a hybrid of two previous studies: the P wave velocity in the crust shallower than 10 km is based on a refraction experiment (Iwasaki et al 2004) and the velocity in the crust deeper than 10 km is based on a seismic tomography analysis (Katsumata et al 2006). The second one is based on a travel time analysis of the aftershocks occurred within 4 hours after the main shock (Katsumata et al 2019). No amplitude data were used.

There are several stress inversion methods to estimate the state of stress from focal mechanisms. Only four independent components are able to be obtained from the stress inversion method: the orientation (trend tr and plunge p /angle) of the axes of three principal stresses and the stress ratio. The trend tr is an azimuthal angle: $tr = 0^\circ, 90^\circ, 180^\circ, \text{ and } 270^\circ$ indicate the north, the east, the south, and the west, respectively. The plunge is measured from the horizontal: $p = 0^\circ$ and 90° indicate horizontal and vertical axes, respectively. The principal stresses are the maximum principal stress (σ_1), the intermediate principal stress (σ_2), and the minimum principal stress (σ_3) and the stress ratio R is defined as $R = (\sigma_1 - \sigma_2) / (\sigma_1 - \sigma_3)$, indicating the relative magnitude of the principal stresses and ranging from 0 to 1. We determined the stress field with a stress inversion method developed by Hardebeck and Michael (2006) using focal mechanisms as input data. The method is performed by dividing the study area sufficiently fine in

advance, putting a constraint that the stress changes smoothly between neighboring areas to avoid instability of the solution, and calculating the stress of all areas at once by using a least squares method. The uncertainty of the parameters is estimated using 2000 bootstrap resampling of all data (Hardebeck and Michael 2006). In this study the two-dimensional nodes are placed in the aftershock area: the latitude ranges from 42.55 to 42.85°N and the grid spacing is 0.05°, the longitude is fixed at 142.0°E for all nodes, and the depth ranges from 8.2 to 45.1 km and the grid spacing is 4.1 km. The focal mechanisms of aftershocks that occurred within 7 km from each node were used. The stress parameters were calculated at nodes with at least 8 focal mechanisms. We selected the damping parameter e (equation (14) in Hardebeck and Michael 2006) based on the trade-off curve between the model length and the data variance. The corner of the trade-off curve was near $e \approx 1.2$, so we selected $e = 1.2$ for all groups in this study.

Results

Focal mechanisms

We determined 818 focal mechanisms from 1785 aftershocks. Details of all focal mechanisms are given in the supplementary material (see Additional file 2). The number of polarity data ranged from 8 to 80, and its average was about 30. There were 591 focal mechanisms with more than 20 first motion polarities. The nodal plane uncertainty ranged from 8° to 55°, and the average uncertainty for the 1636 (= 818 × 2) nodal planes of the 818 focal mechanisms was 27°. We evaluated the quality of the determined focal mechanisms as A, B, C or D based on its estimation accuracy according to Hardebeck and Sherer (2002). Quality A and D solutions have the highest and lowest levels of quality, respectively. The number of focal mechanisms of Qualities A, B, C, and D were 314, 231, 130, 143, respectively. In this study, we use the 545 focal mechanisms of Qualities A and B in the following analyses (Fig. 4). The nodal plane uncertainty of these mechanisms ranges from 8° to 42°, and the average for the 1090 (=545 × 2) nodal planes of the 545 focal mechanisms is 22°.

The averages of the trends of the P- and T-axes are $tr = 78^\circ \pm 33^\circ$ and $357^\circ \pm 52^\circ$, respectively, for all 545 focal mechanisms of Quality A and B (Fig. 5). The averages of the plunges of the P- and T-axes are $pl = 25^\circ \pm 16^\circ$ and $46^\circ \pm 20^\circ$, respectively. The T-axes have a larger plunge than the P-axes. These variations of the P- and T-axes come from the variations in the focal mechanisms. Triangle diagrams (Frohlich 2001) show the distribution of focal mechanisms based on the plunge of the P-, T-, and B-axes (Fig. 6). In the study area, most focal mechanisms are classified into reverse fault, strike-slip fault, and other type's earthquakes, and few focal mechanisms are classified into normal fault earthquakes.

Orientation of principal stresses

We obtained the stress parameters at 44 nodes in the aftershock area of the 2018 Hokkaido Eastern Iwate earthquake. The calculated values at each node are given in the supplementary material (see Additional file 3). The mean and the standard deviation of the parameters at the 44 nodes were calculated (Fig. 7

and Table 1). We found that the axis of σ_1 is oriented to ENE-WSW and the axis of σ_1 is close to be horizontal or tilting down to the eastward. The fault plane of the main shock dips approximately 70° eastward (Kobayashi T et al 2019; Guo et al 2019). The $p/ = 17^\circ$ of σ_1 may promote the slip of the main shock. We also found that the axis of σ_3 is close to be vertical. Therefore, the results strongly suggest that the reverse fault type stress field is dominant, and the near-horizontal compressional stress is acting in the ENE-WSW direction in the aftershock area of the 2018 Hokkaido Eastern Iburi earthquake. According to JMA (2018a), the orientation of P- and T-axes of the CMT solution of the main shock are $tr = 67^\circ$ and 274° , respectively, and the plunge of P- and T-axes are $p/ = 17^\circ$ and 71° , respectively. Therefore, the stress field obtained in this study is consistent with the CMT solution of the main shock.

The vertical cross sections are shown in Fig. 8. The mean trend of σ_1 -axis is 73° and there is no remarkable spatial change in trend (Fig. 8a). On the other hand, there are remarkable spatial changes in the plunge of σ_1 -axis (Fig. 8b). The mean plunge of σ_1 -axis is 17° . The plunge is deviated by approximately 10° in the direction that the plunge becomes horizontal in the portion shallower than 20 km and the plunge is deviated by approximately 10° in the direction that plunge becomes vertical in the portion deeper than 20 km. A similar tendency is seen in the plunge of σ_3 -axis (Fig. 8d). In the case of the trend of σ_3 -axis, the spatial pattern changes at a depth of 30 km rather than 20 km (Fig. 8c).

Depth dependence of the stress ratio R

When the 44 nodes were averaged, the stress ratio R was 0.6 (Table 1). The estimated value of R at each node has a very large error (see Additional file 3). The difference in the values between the nodes falls within the error range, and it cannot be said that there is a statistically significant difference. Therefore, the following judgment is reasonable: it is futile to discuss further the spatial pattern of stress ratios. Although we know that there is no statistical significance, we dare to propose a hypothesis that R may have depth dependence in this study.

There seems to be depth dependence: R decreases systematically from the shallow to the deep portions (Fig. 9). Ohtani and Imanishi (2019) conducted a stress inversion using 27 focal mechanisms of aftershocks. Almost all hypocenters are located within 7 km from a node at 42.7°N and 24.6 km in depth. The depth of hypocenters determined by Ohtani and Imanishi (2019) might be shallower by 3-4 km systematically than those determined in the present study due to difference in the velocity structure of P wave. In the present study, the stress ratio was estimated to be 0.5 at this node (42.7°N , 24.6 km) with the error range from 0.33 to 0.86. Therefore, there will be no significant difference between the results obtained by Ohtani and Imanishi (2019) and the results in this study.

To express the depth dependency quantitatively, we estimated a best-fitted curve of R as a function of the depth. The nodes in the depth direction are located from a depth of 8.2 km to 45.1 km with an interval of 4.1 km. We calculated the average value of R at each depth (Fig. 10a). By fitting the polynomials of 0th to 3rd to the average value of R , AIC was calculated, and the optimal order of the polynomial was determined:

$$R = \sum_{n=0}^m a_n z^n \quad (m = 0, 1, 2, 3) \quad (1),$$

where R is the stress ratio averaged at each depth and z is the depth in km. The result of the polynomial fitting to R was shown on Table 2. AIC is the smallest when $m = 2$, therefore the depth dependence of R is not linear but quadratic.

The maximum shear stress is defined as $\tau_{\max} = (\sigma_1 - \sigma_3) / 2$. Based on the depth dependency of R , we estimated τ_{\max} as a function of depth with assumptions as follows: (1) R is given by a quadratic polynomial of depth as described above, (2) the minimum principal stress σ_3 is equal to the lithostatic overburden pressure minus hydrostatic pressure, $\sigma_3(z) = 16.7 z$ (MPa) at z km depth (e.g. Aochi and Ulrich 2015; Ando and Kaneko 2018; Hisakawa et al 2020), and (3) $\sigma_2 \approx \sigma_3$ (Hisakawa et al 2020) in this case we assumed $\sigma_2 = 1.01 \sigma_3$. As a result of a simple arithmetic calculation, τ_{\max} monotonically increases up to a depth of 27 km, reaches a maximum value, and then decreases below 27 km (Fig. 10b). Note that the important point is not the absolute value of τ_{\max} , but the change pattern of increase/maximum value/decrease. The absolute value depends on how you suppose the relationship between σ_2 and σ_3 .

Discussion

Reverse-faulting stress field in the western boundary of the HCZ

In this study, the state of stress was revealed in the aftershock area of the 2018 Hokkaido Eastern Iburi earthquake ($M_{\text{JMA}} = 6.7$) which is in the western boundary of the Hidaka Collision Zone (HCZ). The state of stress revealed by a stress inversion analysis of the aftershocks showed that the dominant stress field is the reverse fault type, the σ_1 -axis is in the direction of ENE-WSW, i.e., $tr = 73^\circ$, and the σ_1 -axis is close to be horizontal. The direction of ENE-WSW is clearly different from the convergence direction of the PA plate. Therefore, a model that the compressional stress field due to the collision extends to the western boundary of the HCZ is strongly supported by not only the CMT solution of the 2018 main shock but also the focal mechanisms of its aftershocks.

Terakawa and Matsu'ura (2010) insisted that the stress field of reverse faulting type is dominant in the aftershock area of the 2018 Hokkaido Eastern Iburi earthquake: the axis of σ_1 is close to be horizontal with almost EW direction and the axis of σ_3 is near-vertical. The results obtained in this study are consistent with those obtained by Terakawa and Matsu'ura (2010). Kita et al (2012) applied a stress inversion analysis to focal mechanisms of small earthquakes occurred in and around an area 100 km east of the 2018 main shock. As a result, they found that the trend and the plunge of σ_1 -axis are 224° and 20° , respectively. The trend of σ_1 -axis obtained by Kita et al (2012) is different from that obtained in this study. This difference might suggest the stress field is not uniform in the HCZ.

Possible causes of stress inhomogeneity

In this study we suggested that the stress ratio R decreases as a quadratic polynomial of depth from 8 to 45 km and this change is due to the maximum shear stress τ_{\max} that increases from 8 to 27 km and decreases from 27 to 45 km. There are three possible causes of the stress inhomogeneity. The first one is change in materials around the Moho discontinuity. The depth of the Moho was estimated to be approximately 30 km in the aftershock area of the 2018 Hokkaido Eastern Iburi earthquake (Yoshii 1972; Matsubara et al 2017). The change of τ_{\max} at a depth of 27 km from increase to decrease seems to be related to the Moho. However, mantle materials have a higher rigidity than crustal materials in general, and thus it is unlikely that the shear stress will suddenly decrease in the mantle. The second one is the brittle-ductile transition. The temperature was estimated to be approximately 400 °C at a depth of 30 km in the aftershock area and this temperature is lower than the solidus temperature (Nishida and Hashimoto 2007).

The third one is the coseismic slip during the main shock. Many authors pointed out that aftershocks concentrate not within the large coseismic slip area but in its surrounding area (e.g. Mendoza and Hartzell 1988; Beroza and Zoback 1993; Das and Henry 2003; Hsu et al. 2006; Woessner et al. 2006; Perfettini et al. 2010; Asano et al. 2011; Kato and Igarashi 2012). These observations strongly suggest that aftershocks are induced by the local accumulation of the shear stress due to the rupture of main shock. There is an area where the R value is much larger than the value expected from the quadratic function: $R = 0.92$ at a node A (42.60°N, 28.7 km) and $R = 0.82$ at a node B (42.55°N, 28.7 km) (Fig. 9). The nodes A and B are in the southern part of the aftershock area. Some authors have reported that the coseismic slip is much larger in the southern part than in the northern part of the aftershock area (Kobayashi H et al 2019; Asano and Iwata 2019). Asano and Iwata (2019) analyzed the strong-motion data by using a kinematic waveform inversion method and found that the peak slip of 1.7 m was located at a depth of about 26 km, southwest of the epicenter. This large slip area matches well with the large R value area at the nodes A and B. This correlation was also observed in the 2008 Iwate-Miyagi Nairiku earthquake, which was a reverse-fault-type earthquake (personal communications with Keisuke Yoshida). Hisakawa et al (2020) conducted a dynamic rupture simulation of the 2018 Hokkaido Eastern Iburi earthquake, and showed that the shear stress rise of 10 - 15 MPa is possible theoretically near the boundary on the deep side of the large coseismic slip area. The τ_{\max} estimated in the aftershock area reaches the maximum around this deeper boundary and the aftershock is concentrated below this deeper boundary. The coseismic slip seems to best explain the depth dependence of τ_{\max} .

Conclusions

We deployed temporary seismic stations immediately after the main shock of the 2018 Hokkaido Eastern Iburi earthquake ($M_{\text{JMA}} = 6.7$). The dense seismic stations enabled us to determine focal mechanism solutions accurately by using the first motion polarity of P wave. A stress inversion method was applied to the focal mechanism solutions to investigate the state of stress in the aftershock area. Looking at the

stress field in the aftershock area in detail, the orientation of σ_1 - and σ_3 -axes seemed to slightly depend on the depth. Moreover, what is interesting is the depth dependence of the stress ratio R . Although the statistical significance is very poor, we dare to present a model that the R value is a quadratic polynomial of depth, indicating the change in shear stress that has a maximum around 27 km in depth. Although the coseismic slip seems to best explain the depth dependence of the shear stress, this model is a hypothesis to examine in future works.

Declarations

Availability of data and materials

The datasets used and/or analyzed during the current study are available from the corresponding author on reasonable request.

Competing interests

The authors declare that they have no competing interests.

Funding

This study was partly supported by the Ministry of Education, Culture, Sports, Science and Technology (MEXT) of Japan, under its “The Second Earthquake and Volcano Hazards Observation and Research Program (Earthquake and Volcano Hazard Reduction Research)”. This study was also partly supported by MEXT KAKENHI grant 18K19952.

Authors' contributions

YS determined the focal mechanisms and conducted the stress inversion. KK was a major contributor in writing the manuscript. MI read all arrival times of P and S waves and the first motion polarity of P wave. MO, HA, RT, MT, TY, KO, and HT are the technical staff members who maintain the seismic stations of Hokkaido University and the temporary seismic stations. SS, SM, TO, TM, HM, SH, YY, SH, MK, HK, YI, AN, NT, TU, and members of the Group for the Aftershock Observations are important persons to maintain the temporary seismic stations. All authors read and approved the final manuscript.

Acknowledgements

We thank Takuya Nishimura, Andrew Michael, and an anonymous reviewer for valuable comments. We thank Toshiko Terakawa for valuable discussions. We used waveform data from seismic stations maintained by JMA, and we also used waveform data from High-Sensitivity Seismograph Network of Japan (Hi-net) maintained by NIED. We used observation equipment at some seismic stations supported by the Earthquake Research Institute Joint Usage/Research Program 2016-F2-02, 2017-F2-02, 2018-F2-02, 2019-F2-02, and 2020F2-02. GMT-SYSTEM (Wessel and Smith 1991) was used for mapping data.

A list of individual members of the Group for the Aftershock Observations of the 2018 Hokkaido Eastern Iburi Earthquake follows: Yuki Susukida^{1,11}, Kei Katsumata¹, Masayoshi Ichianagi¹, Mako Ohzono¹, Hiroshi Aoyama¹, Ryo Tanaka¹, Masamitsu Takada¹, Teruhiro Yamaguchi¹, Kazumi Okada¹, Hiroaki Takahashi¹, Shin'ichi Sakai², Koji Miyakawa², Shin'ichi Tanaka², Miwako Ando², Satoshi Matsumoto³, Tomomi Okada⁴, Toru Matsuzawa⁴, Naoki Uchida⁴, Ryosuke Azuma⁴, Ryota Takagi⁴, Keisuke Yoshida⁴, Takashi Nakayama⁴, Satoshi Hirahara⁴, Toshiko Terakawa⁵, Yoshiko Yamanaka⁵, Yuta Maeda⁵, Shinichiro Horikawa⁵, Hiroki Miyamachi⁶, Shuichiro Hirano⁶, Hiroshi Yakiwara⁶, Masahiro Kosuga⁷, Takuto Maeda⁷, Hiroshi Katao⁸, Yoshihisa Iio⁸, Airi Nagaoka⁸, Noriko Tsumura⁹, Masahiro Shimazaki⁹, Tomotake Ueno¹⁰, and Youichi Asano¹⁰, where ¹ Hokkaido University, ² University of Tokyo, ³ Kyushu University, ⁴ Tohoku University, ⁵ Nagoya University, ⁶ Kagoshima University, ⁷ Hirosaki University, ⁸ Kyoto University, ⁹ Chiba University, ¹⁰ National Research Institute for Earth Science and Disaster Resilience and ¹¹ KOZO KEIKAKU ENGINEERING Inc., Tokyo, Japan

References

1. Ando R, Kaneko Y (2018) Dynamic rupture simulation reproduces spontaneous multifault rupture and arrest during the 2016 M_w 7.9 Kaikoura earthquake. *Geophys Res Lett* 45:12875–12883. doi:10.1029/2018gl080550
2. Aochi H, Ulrich T (2015) A probable earthquake scenario near Istanbul determined from dynamic simulations. *Bull Seismol Soc Am* 105(3):1468–1475. doi:10.1785/0120140283
3. Arita K, Ganzawa Y, Itaya T (2001) Tectonics and uplift process of the Hidaka Mountains, Hokkaido, Japan inferred from thermochronology [in Japanese with English figure captions]. *Bull Earthq Res Inst Univ Tokyo* 76:93-104.
4. Asano K, Iwata T (2019) Source rupture process of the 2018 Hokkaido Eastern Iburi earthquake deduced from strong-motion data considering seismic wave propagation in three-dimensional velocity structure. *Earth Planets Space* 71:101. doi:10.1186/s40623-019-1080-0
5. Asano Y, Saito T, Ito Y, Shiomi K, Hirose H, Matsumoto T, Aoi S, Hori S, Sekiguchi S (2011) Spatial distribution and focal mechanisms of aftershocks of the 2011 off the Pacific coast of Tohoku earthquake, *Earth Planets Space* 63:669-673. doi:10.5047/eps.2011.06.016
6. Beroza G C, Zoback M D (1993) Mechanism diversity of Loma Prieta aftershocks and the mechanics of mainshock-aftershock interaction. *Science* 259:210-213. doi:10.1126/science.259.5092.210
7. Bird P (2003) An updated digital model of plate boundaries. *Geochemistry, Geophysics, Geosystems* 4(3):1027. doi:10.1029/2001GC000252
8. Das S, Henry C (2003) Spatial relation between main earthquake slip and its aftershock distribution. *Rev Geophys* 41(3):1013. doi:10.1029/2002RG000119.
9. DeMets C (1992) Oblique convergence and deformation along the Kuril and Japan Trenches. *J Geophys Res* 97:17615-17625. doi:10.1029/92JB01306.

10. DeMets C, Gordon R G, Argus D F, Stein S (1994) Effect of recent revisions to the geomagnetic reversal time scale on estimates of current plate motions. *Geophys Res Lett* 21:2191-2194. doi:10.1029/94GL02118
11. Frohlich C (2001) Display and quantitative assessment of distributions of earthquake focal mechanisms. *Geophys J Int* 144:300–308. doi:10.1046/j.1365-246x.2001.00341.x.
12. Guo Z et al (2019) Fault Slip Model of the 2018 Mw 6.6 Hokkaido Eastern Iburi, Japan, Earthquake Estimated from Satellite Radar and GPS Measurements. *Remote Sensing* 11:1667. doi:10.3390/rs11141667
13. Hardebeck J L, Shearer P M (2002) A new method for determining first-motion focal mechanisms. *Bull Seism Soc Am* 92:2264-2276. doi:10.1785/0120010200.
14. Hardebeck JL, Michael AJ (2006) Damped regional-scale stress inversions: Methodology and examples for southern California and the Coalinga aftershock sequence. *J Geophys Res* 111:B11310. doi:10.1029/2005JB004144.
15. Hashimoto C, Noda A, Sagiya T et al (2009) Interplate seismogenic zones along the Kuril–Japan trench inferred from GPS data inversion. *Nature Geosci* 2:141-144. doi:10.1038/ngeo421
16. Hirata N, Matsu'ura M (1987) Maximum-likelihood estimation of hypocenter with origin time eliminated using nonlinear inversion technique. *Phys Earth Planet Inter* 47:50-61. doi:10.1016/0031-9201(87)90066-5.
17. Hisakawa T, Ando R, Yano T E et al (2020) Dynamic rupture simulation of 2018, Hokkaido Eastern Iburi earthquake: role of non-planar geometry. *Earth Planets Space* 72:36. doi:10.1186/s40623-020-01160-y.
18. Hsu Y J et al (2006) Frictional afterslip following the 2005 Nias-Simeulue earthquake, Sumatra. *Science* 312:1921-1926. doi:10.1126/science.1126960.
19. Hua YY, Zhao DP, Xu YX, Wang ZW (2019) Arc-arc collision caused the 2018 Eastern Iburi earthquake (M 6.7) in Hokkaido, Japan. *Scientific Reports* 9:13914. doi:10.1038/s41598-019-50305-x
20. Ito T et al (1999) Delamination wedge structure beneath the Hidaka collision zone [in Japanese]. *Chikyū Monthly* 21(3):130-136.
21. Iwasaki T et al (2004) Upper and middle crustal deformation of an arc-arc collision across Hokkaido, Japan, inferred from seismic refraction/wide-angle reflection experiments. *Tectonophysics* 388:59-73. doi:10.1016/j.tecto.2004.03.025.
22. JMA (2018a) The CMT solutions. <https://www.data.jma.go.jp/svd/eqev/data/mech/cmt/fig/cmt20180906030759.html>. Accessed 16 June 2020.
23. JMA (2018b) Focal mechanism solutions by using first motion polarities. <https://www.data.jma.go.jp/svd/eqev/data/mech/ini/fig/mc20180906030759.html>. Accessed 16 June 2020.

24. Kasahara M, Kodaira S, Motoya Y (1994) Aftershock distribution of the 1993 Kushiro-oki earthquake and the seismicity in and around Hokkaido before the main shock. Research report on the damages from the 1993 Kushiro-oki earthquake:27-34. Supported by the Japanese Ministry of Education, Science, Sport and Culture (Grant No. 04306025).
25. Kato A, Igarashi T (2012) Regional extent of the large coseismic slip zone of the 2011 M_w 9.0 Tohoku-Oki earthquake delineated by on-fault aftershocks. *Geophys Res Lett* 39:L15301. doi:10.1029/2012GL052220.
26. Katsumata K et al (2002) Distribution of hypocenters and focal mechanisms in and around the Hidaka arc-arc collision zone revealed by a dense temporary seismic network. *Bull Earthq Res Inst Univ Tokyo* 77:199-223.
27. Katsumata K, Wada N, Kasahara M (2003) Newly imaged shape of the deep seismic zone within the subducting Pacific plate beneath the Hokkaido corner, Japan-Kurile arc-arc junction. *J Geophys Res* 108(B12):2565. doi:10.1029/2002JB002175.
28. Katsumata K, Wada N, Kasahara M (2006) Three-dimensional P and S wave velocity structures beneath the Hokkaido corner, Japan-Kurile arc-arc junction. *Earth Planets Space* 58:e37–e40. doi:10.1186/BF03352595.
29. Katsumata K, Ichiyanagi M, Ohzono M et al (2019) The 2018 Hokkaido Eastern Iburi earthquake ($M_{JMA} = 6.7$) was triggered by a strike-slip faulting in a stepover segment: insights from the aftershock distribution and the focal mechanism solution of the main shock. *Earth Planets Space* 71: 53. doi:10.1186/s40623-019-1032-8.
30. Kimura G (1981) Tectonic evolution and stress field in the southwestern margin of the Kurile Arc. *J Geol Soc Japan* 87:757-768. doi:10.5575/geosoc.87.757.
31. Kimura G (1986) Oblique subduction and collision: Forearc tectonics of the Kurile arc. *Geology* 14:404-407. doi:10.1130/0091-7613(1986)14<404:OSACFT>2.0.CO;2.
32. Kimura G (1996) Collision orogeny at arc-arc junctions in the Japanese Islands. *Island Arc* 5:262-275. doi:10.1111/j.1440-1738.1996.tb00031.x.
33. Kita S, Hasegawa A, Nakajima J, Okada T, Matsuzawa T, Katsumata K (2012) High-resolution seismic velocity structure beneath the Hokkaido corner, northern Japan: Arc-arc collision and origins of the 1970 M 6.7 Hidaka and 1982 M 7.1 Urakawa-oki earthquakes. *J Geophys Res* 117:B12301. doi:10.1029/2012JB009356.a
34. Kobayashi H, Koketsu K, Miyake H (2019) Rupture process of the 2018 Hokkaido Eastern Iburi earthquake derived from strong motion and geodetic data. *Earth Planets Space* 71:63. doi:10.1186/s40623-019-1041-7
35. Kobayashi T, Hayashi K, Yurai H (2019) Geodetically estimated location and geometry of the fault plane involved in the 2018 Hokkaido Eastern Iburi earthquake. *Earth Planets and Space* 71:62. doi:10.1186/s40623-019-1042-6
36. Matsubara M, Sato H, Ishiyama T, Horne A V (2017) Configuration of the Moho discontinuity beneath the Japanese Islands derived from three-dimensional seismic tomography. *Tectonophysics* 710-

- 711:97-107. doi:10.1016/j.tecto.2016.11.025
37. Mendoza C, Hartzell S H (1988), Aftershock patterns and main shock faulting. *Bull Seismol Soc Am* 78(4): 1438–1449.
 38. Moriya T (1972) Aftershock activity of the Hidaka Mountains earthquake of January 21, 1970 [in Japanese with English figure captions]. *J Seismol Soc Japan* 24:287–297. doi:10.4294/zisin1948.24.4_287.
 39. Moriya T (1986) Collision of forearcs and the overlapped deep seismic zone in the transitional zone between the northern Honshu and Kurile arcs. *J Phys Earth* 34:S175-S192. doi:10.4294/jpe1952.34.Supplement_S175.
 40. Moriya T (1999) Seismicity associated with the triple collision structure in the southern part of the Hidaka Mountain Range, Hokkaido, Japan [in Japanese]. *Chikyu Monthly Extra* 27:206-210.
 41. Moriya T, Miyamachi H, Katoh S (1983) Spatial distribution and mechanism solutions for foreshocks, mainshock and aftershocks of the Urakawa-oki Earthquake of March 21, 1982 [in Japanese with English figure captions]. *Geophys Bull Hokkaido Univ* 42:191–213. doi:10.14943/gbhu.42.191.
 42. Moriya et al (1998) Collision structure in the upper crust beneath the southwestern foot of the Hidaka Mountains, Hokkaido, Japan as derived from explosion seismic observations. *Tectonophysics* 290:181-196. doi:10.1016/S0040-1951(98)00011-0.
 43. Motoya Y, Kitagamae M (1971) Report on the earthquake of southern part of Hokkaido on January 21, 1970 [in Japanese with English figure captions]. *Geophys bull Hokkaido Univ* 25:141-153. doi:10.14943/gbhu.25.141.
 44. Murai Y et al (2003) Delamination structure imaged in the source area of the 1982 Urakawa-oki earthquake. *Geophys Res Lett* 30:1490. doi:10.1029/2002GL016459.
 45. NIED (2018a) Focal mechanisms automatically determined by the AQUA system. http://www.hinet.bosai.go.jp/AQUA/aqua_catalogue.php?y=2018&m=09&LANG=en. Accessed 14 April 2020.
 46. NIED (2018b) Recent Large Earthquakes. Tsukuba <http://www.hinet.bosai.go.jp/backnumber/?LANG=en&y=2018&m=09>. Accessed 14 April 2020.
 47. Nishida Y, Hashimoto T (2007) Geothermal structure of the crust and the upper mantle in Hokkaido, Japan: A review [in Japanese with English figure captions]. *Geophys Bull Hokkaido Univ* 70: 1-12. doi: 10.14943/gbhu.70.1
 48. Ohtani M, Imanishi K (2019) Seismic potential around the 2018 Hokkaido Eastern Iburi earthquake assessed considering the viscoelastic relaxation. *Earth Planets and Space* 71:57. doi:10.1186/s40623-019-1036-4
 49. Ozel O et al (1996) Crustal structure in the central Hokkaido, Japan, from a seismic refraction experiment. *J Fac Sci Hokkaido Univ Series 7 Geophys* 10:31-52. <http://hdl.handle.net/2115/8808>.
 50. Perfettini H et al (2010) Seismic and aseismic slip on the central Peru megathrust. *Nature* 465:78–81. doi:10.1038/nature09062.

51. Research Group for Active Faults in Japan (1991) Active Faults in Japan: Sheet Maps and Inventories. Univ of Tokyo Press, Tokyo.
52. Seno T (1985) Northern Honshu microplate hypothesis and tectonics in the surrounding region: When did the plate boundary jump from central Hokkaido to the eastern margin of the Japan Sea?. J Geodetic Soc Japan 31:106-123. doi:[10.11366/sokuchi1954.31.106](https://doi.org/10.11366/sokuchi1954.31.106).
53. Shiina T, Takahashi H, Okada T, Matsuzawa T (2018) Implications of seismic velocity structure at the junction of Kuril-northeastern Japan arcs on active shallow seismicity and deep low-frequency earthquakes. J Geophys Res Solid Earth 123:8732-8747. doi:[10.1029/2018JB015467](https://doi.org/10.1029/2018JB015467)..
54. Takahashi H et al (1999) Velocity field of around the Sea of Okhotsk and Sea of Japan regions determined from a new continuous GPS network data. Geophys Res Lett 26:2533-2536. doi:[10.1029/1999GL900565](https://doi.org/10.1029/1999GL900565).
55. Terakawa T, Matsu'ura M (2010) The 3-D tectonic stress fields in and around Japan inverted from centroid moment tensor data of seismic events. Tectonics 29:TC6008. doi:[10.1029/2009TC002626](https://doi.org/10.1029/2009TC002626)
56. Tsumura N et al (1999) Delamination-wedge structure beneath the Hidaka Collision Zone, Central Hokkaido, Japan inferred from seismic reflection profiling. Geophys Res Lett 26:1057-1060. doi:[10.1029/1999GL900192](https://doi.org/10.1029/1999GL900192).
57. Wessel P, Smith W H F (1991) Free software helps map and display data. Eos Trans AGU 72:445-446.
58. Woessner J, Schorlemmer D, Wiemer S, Mai P M (2006) Spatial correlation of aftershock locations and on-fault main shock properties. J Geophys Res 111:B08301. doi:[10.1029/2005JB003961](https://doi.org/10.1029/2005JB003961).
59. Yoshii T (1972) Terrestrial heat flow and features of the upper mantle beneath the Pacific and the Sea of Japan. J Phys Earth 20:271-285. doi:[10.4294/jpe1952.20.271](https://doi.org/10.4294/jpe1952.20.271).

Tables

Table 1. Principal stresses averaged over the aftershock area.

σ_1	σ_1	σ_2	σ_2	σ_3	σ_3	R
tr (°)	pl (°)	tr (°)	pl (°)	tr (°)	pl (°)	
73 ± 8	17 ± 6	126 ± 91	16 ± 13	289 ± 33	64 ± 9	0.6 ± 0.2

Table 2. Polynomial fitting to the stress ratio R

m	a_0	a_1	a_2	a_3	AIC
0	5.94×10^{-1}				6.113
1	9.26×10^{-1}	-1.25×10^{-2}			0.328
2	7.09×10^{-1}	7.77×10^{-3}	-3.80×10^{-4}		-0.673
3	1.34×10^{-2}	9.72×10^{-2}	-3.71×10^{-3}	3.78×10^{-5}	7.821

Figures

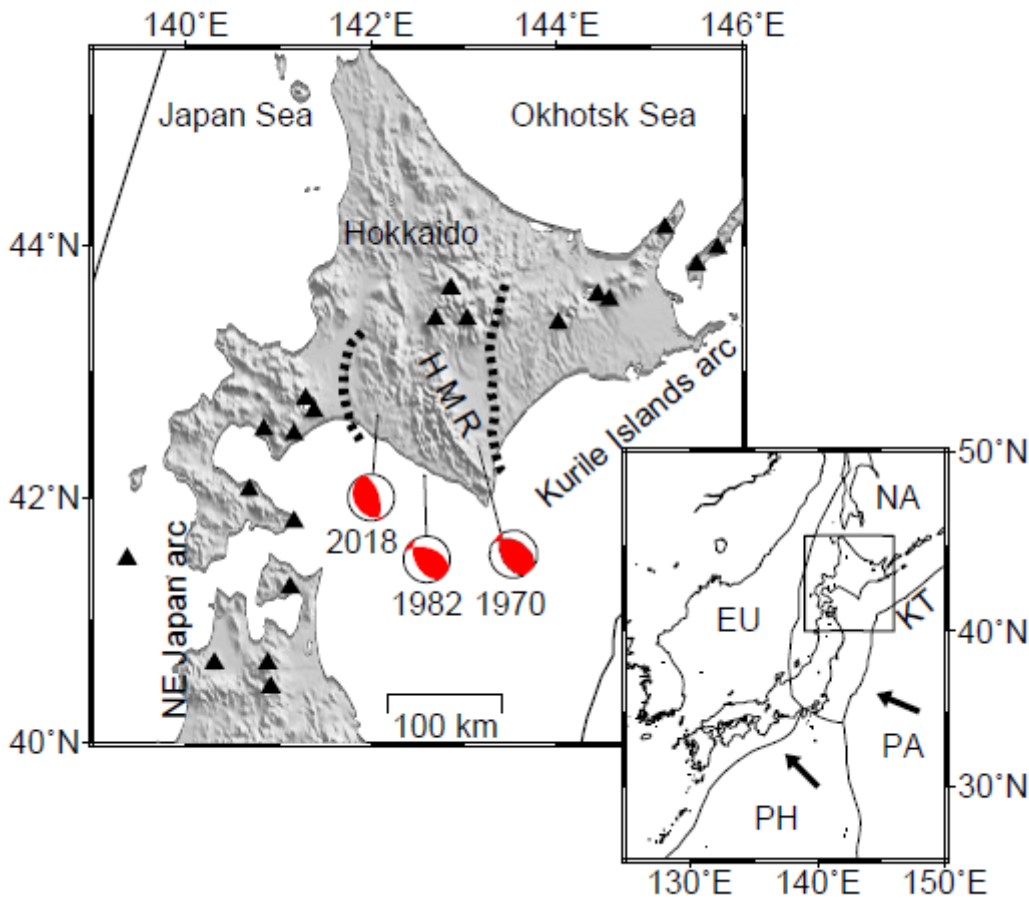


Figure 1

Map showing the Hokkaido corner. Inset shows the plate boundaries (Bird 2003) and the study area in rectangle. The region in and around the Hidaka Mountain Range (HMR) is the Hidaka Collision Zone

(HCZ). Two broken lines show the eastern and the western boundaries of the HCZ. Closed triangles indicate active volcanoes. A red beach ball labeled as 2018 is the centroid moment tensor (CMT) solution of the 2018 Hokkaido Eastern Iburi earthquake (M6.7) (JMA 2018a). A red beach ball labeled as 1982 is the focal mechanism solution of the 1982 Urakawa-oki earthquake (M7.1) by using the first motion polarity of P wave (Moriya et al 1983). A red beach ball labeled as 1970 is the focal mechanism solution of the 1970 Hidaka earthquake (M6.7) by using the first motion polarity of P wave (Kita et al 2012). PA: Pacific plate, PH: Philippine Sea plate, EU: Eurasian plate, NA: North American plate, and KT: Kurile Trench.

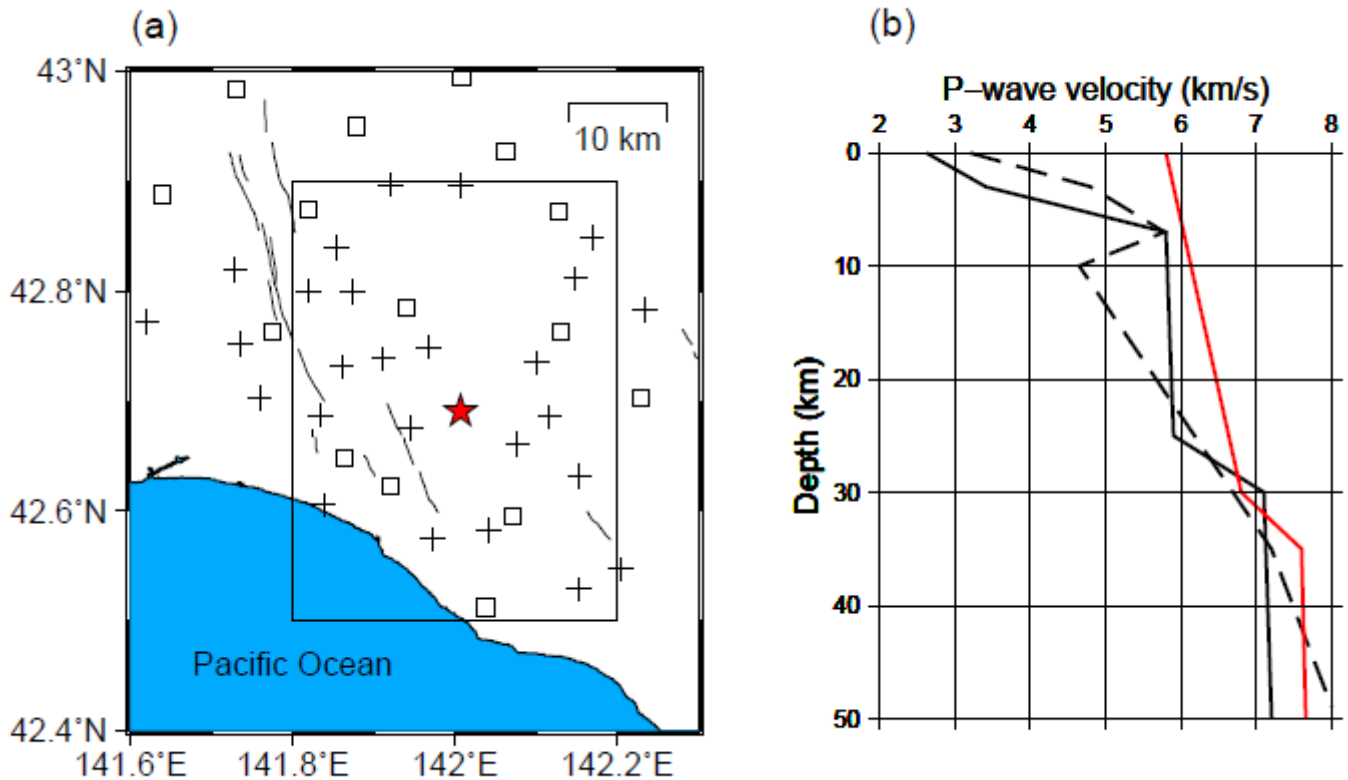


Figure 2

(a) Seismic stations used in this study. Temporary and permanent stations are shown in crosses and in squares, respectively. A red star indicates the epicenter of the main shock of the 2018 Hokkaido Eastern Iburi earthquake. A rectangle indicates an area shown in Fig. 3 - 5. Thin solid lines are active faults (Research Group for Active Faults in Japan 1991). (b) P wave velocity structures. A red line is based on Kasahara et al (1994), a black broken line is based on Iwasaki et al (2004) and Katsumata et al (2006), and a black solid line is based on Katsumata et al (2019).

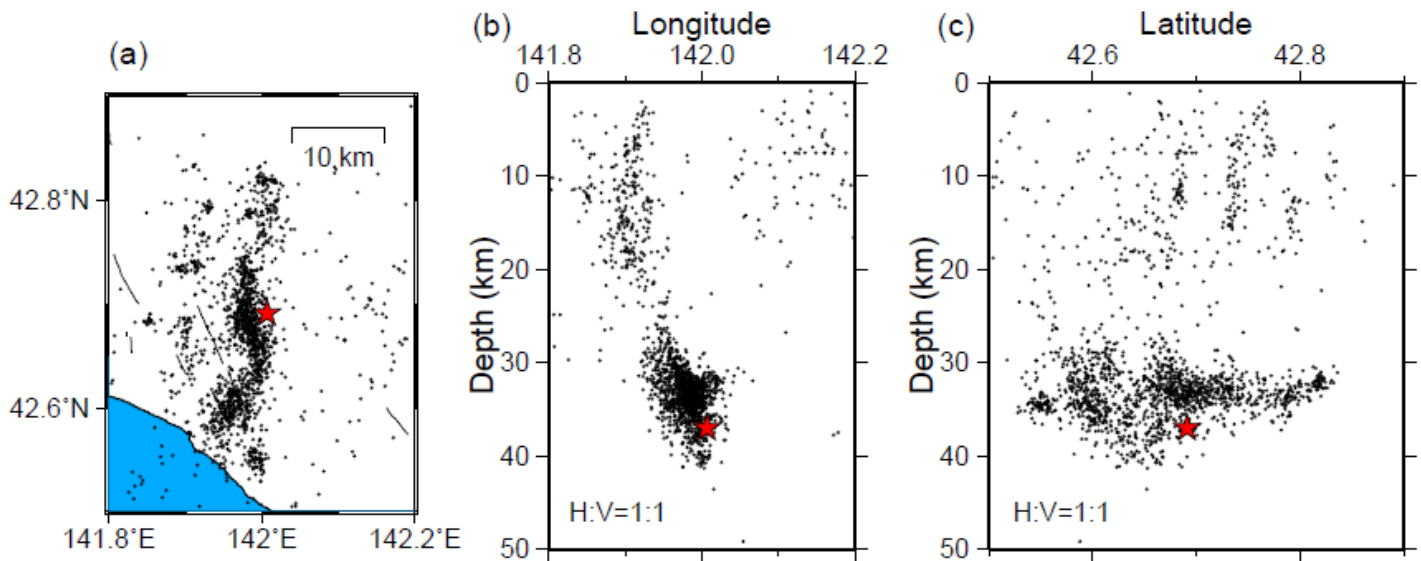


Figure 3

Hypocenter distribution of aftershocks of the 2018 Hokkaido Eastern Iburi earthquake. (a) Epicenter distribution of aftershocks. A red star indicates the epicenter of the main shock. Thin solid lines are active faults (Research Group for Active Faults in Japan 1991). (b) Vertical cross section in East-West. A red star indicates the hypocenter of the main shock. (c) Vertical cross section in North-South. A red star indicates the hypocenter of the main shock.

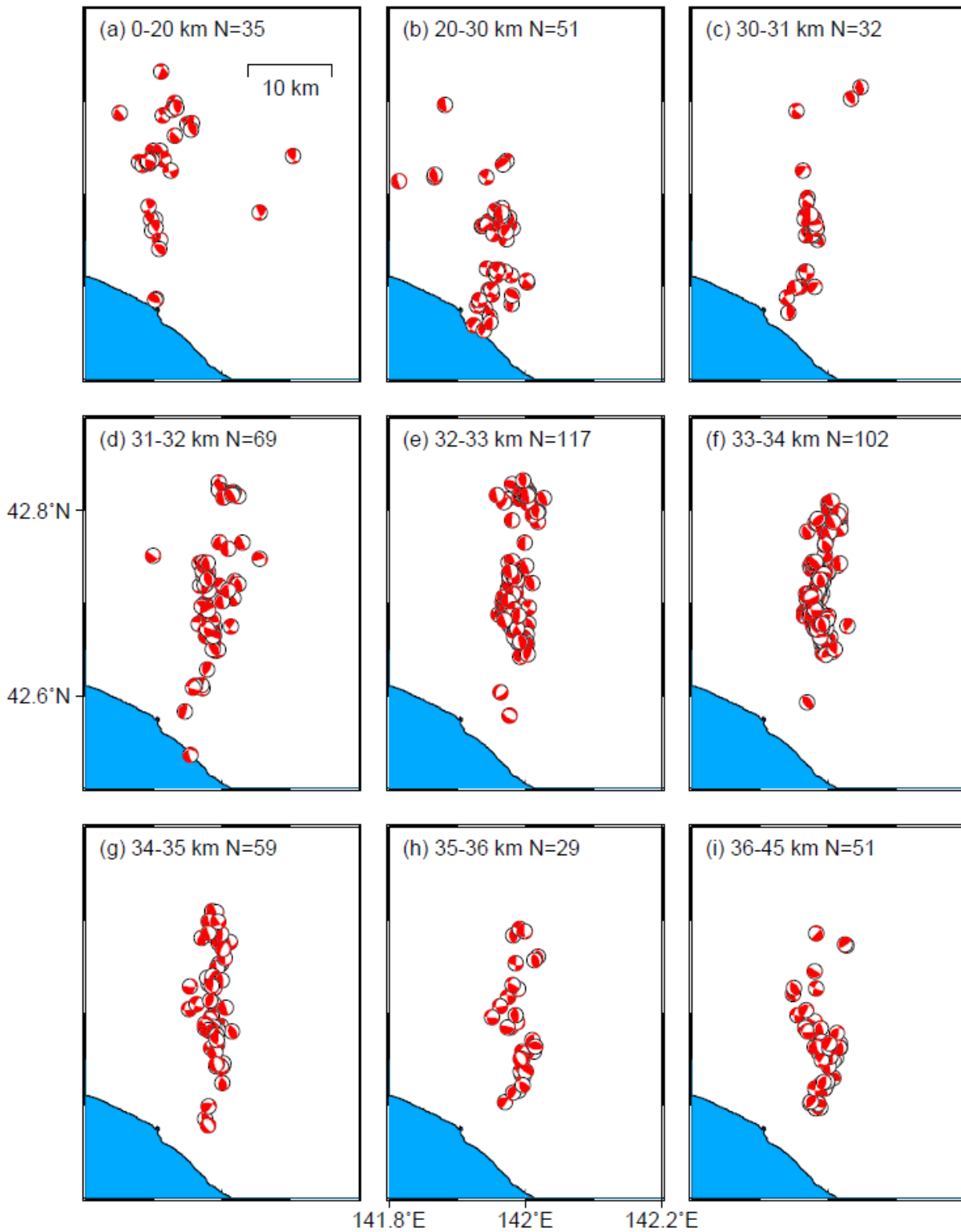


Figure 4

Focal mechanism solutions with Quality A and B determined in this study. The depth of hypocenter is (a) 0-20 km, (b) 20-30 km, (c) 30-31 km, (d) 31-32 km, (e) 32-33 km, (f) 33-34 km, (g) 34-35 km, (h) 35-36 km, and (i) 36-45 km. All diagrams are equal area projections on the lower hemisphere of the focal sphere. Colored areas show compressional quadrants.

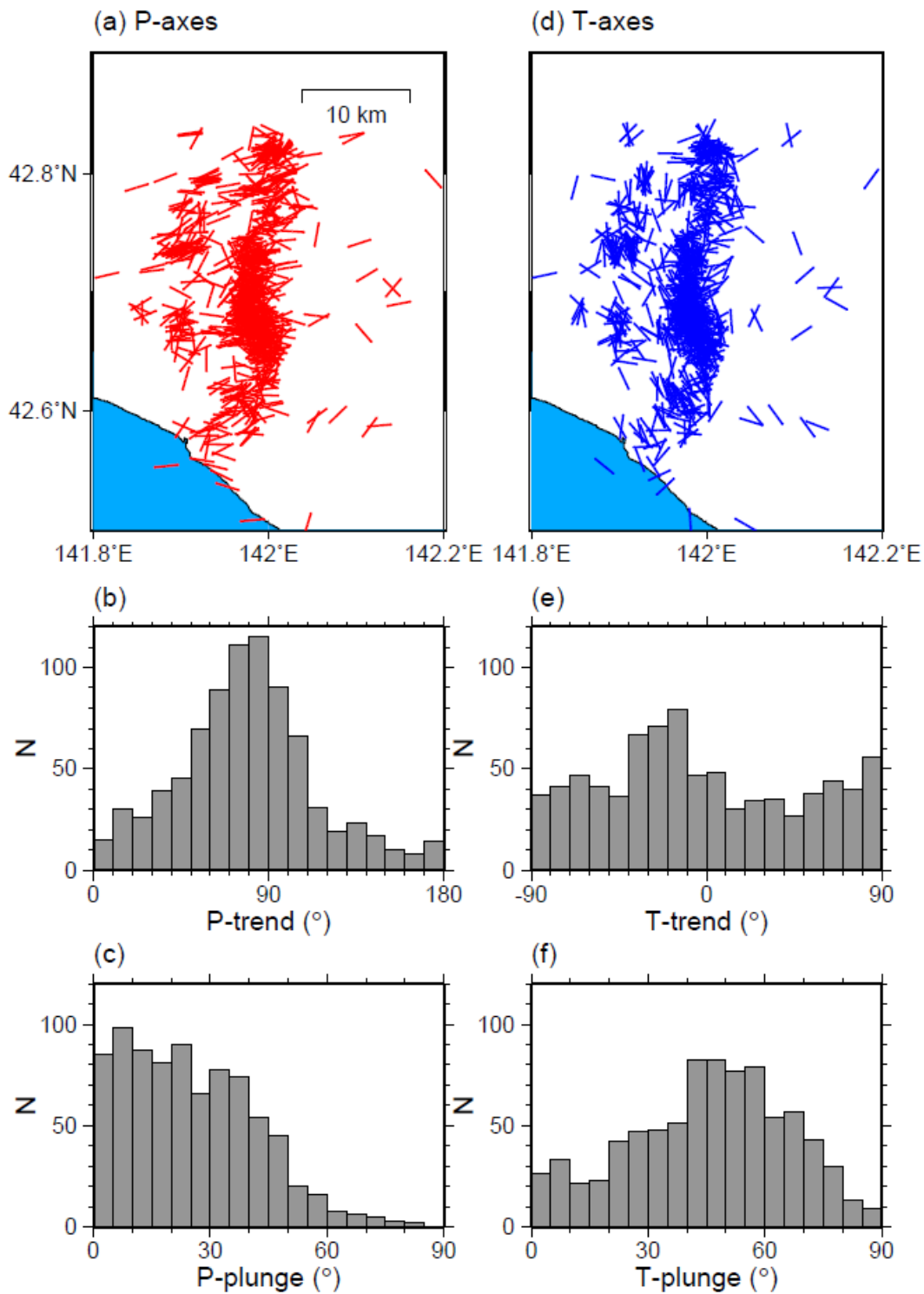


Figure 5

Orientation of (a) P- and (d) T-axes of the focal mechanisms with Quality A and B shown in Fig. 4. Red lines in (a) and blue lines in (d) indicate the trend of the P- and T-axes, respectively. Histograms of the trend of (b) P- and (e) T-axes. Histograms of the plunge of (c) P- and (f) T-axes. The plunge of 0° and 90° indicate horizontal and vertical axes, respectively.

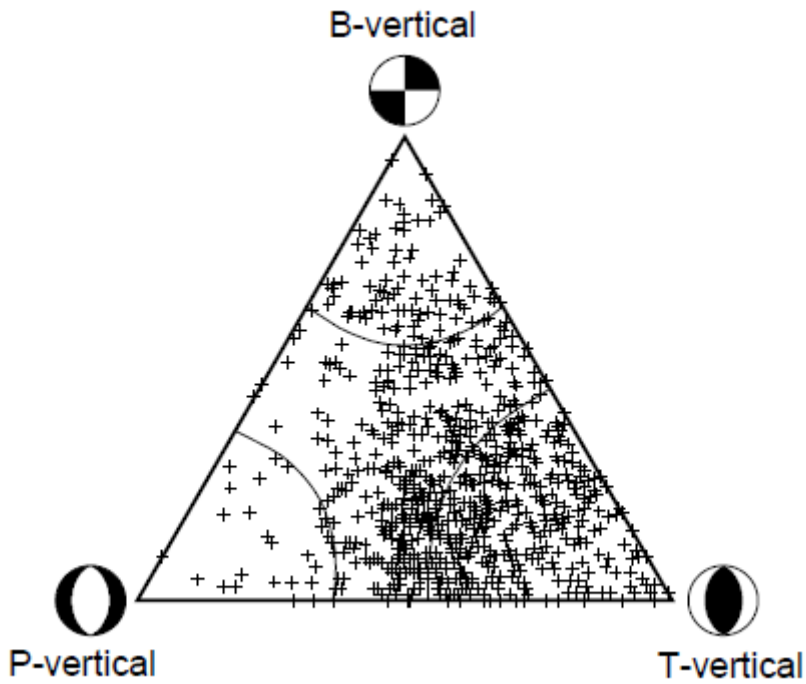


Figure 6

Triangle diagram displaying the distribution of the focal mechanisms with Quality A and B shown in Fig. 4. Curved lines are boundaries with T, B, and P axes of 40°, 30°, and 30° from vertical, respectively (Frohlich 2001).

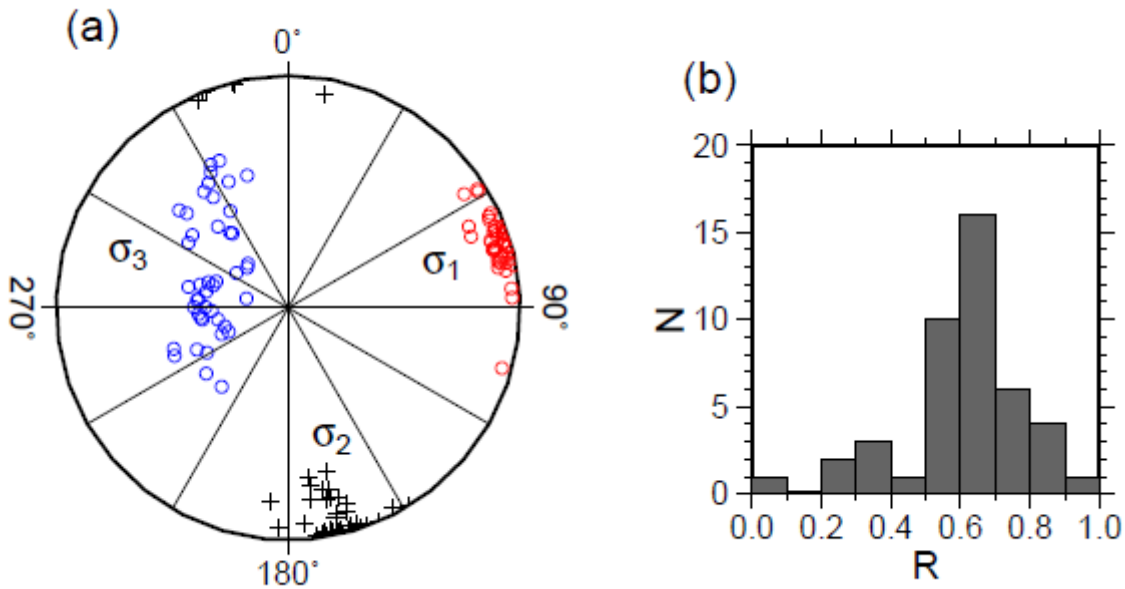


Figure 7

Stress parameters at nodes shown in Fig. 8. (a) the orientation of principal stresses: red circles, crosses, and blue circles indicate σ_1 , σ_2 , and σ_3 at each node, respectively. (b) Histogram of the stress ratio $R =$

$$(\sigma_1 - \sigma_2) / (\sigma_1 - \sigma_3).$$

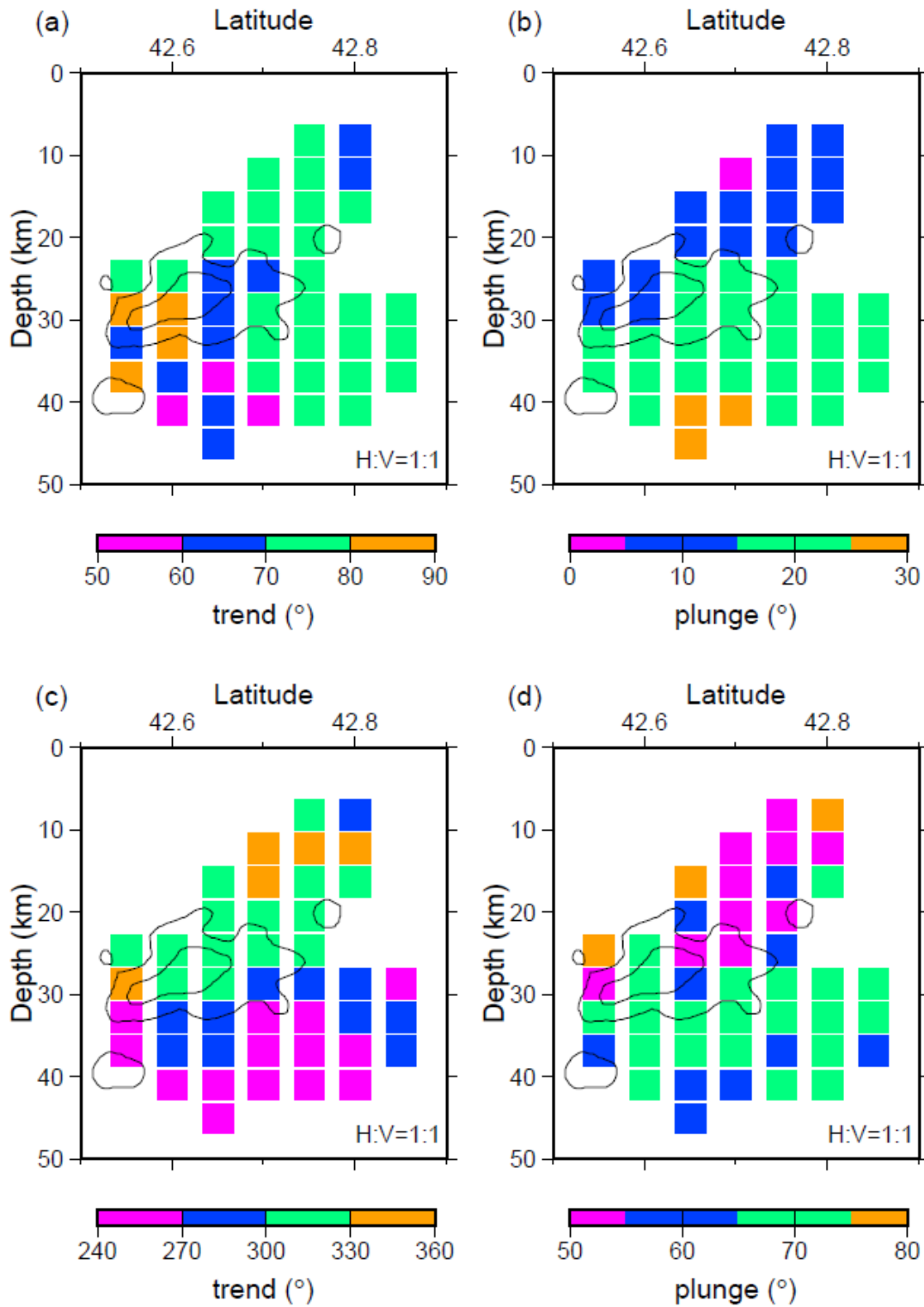


Figure 8

Spatial pattern of the trend and the plunge. (a) the trend of σ_1 -axis, (b) the plunge of σ_1 -axis, (c) the trend of σ_3 -axis, and (d) the plunge of σ_3 -axis. The coseismic slip was indicated by contours with 0.6 and 1.2 m (Asano and Iwata 2019).

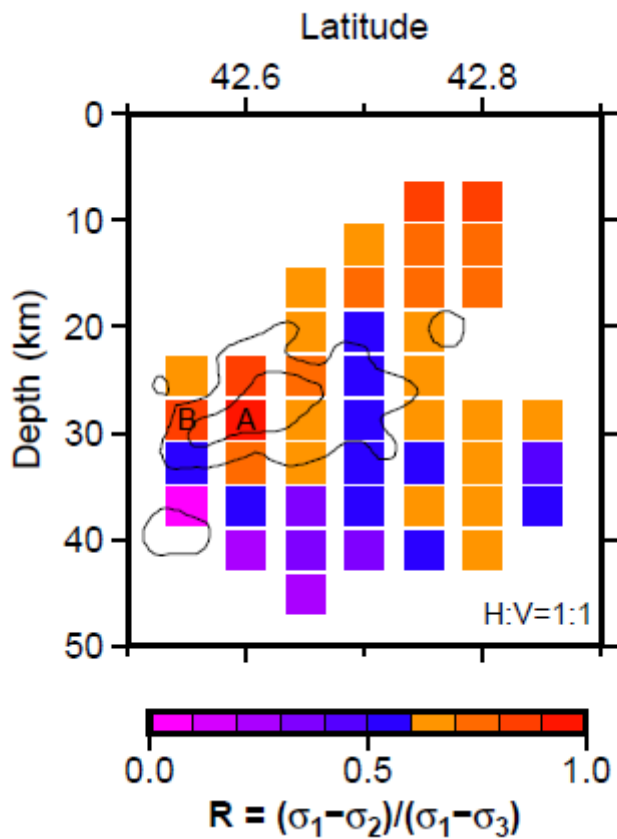


Figure 9

Distribution of the stress ratio R in vertical cross section. A and B represent the nodes with large R -value. The coseismic slip was indicated by contours with 0.6 and 1.2 m (Asano and Iwata 2019).

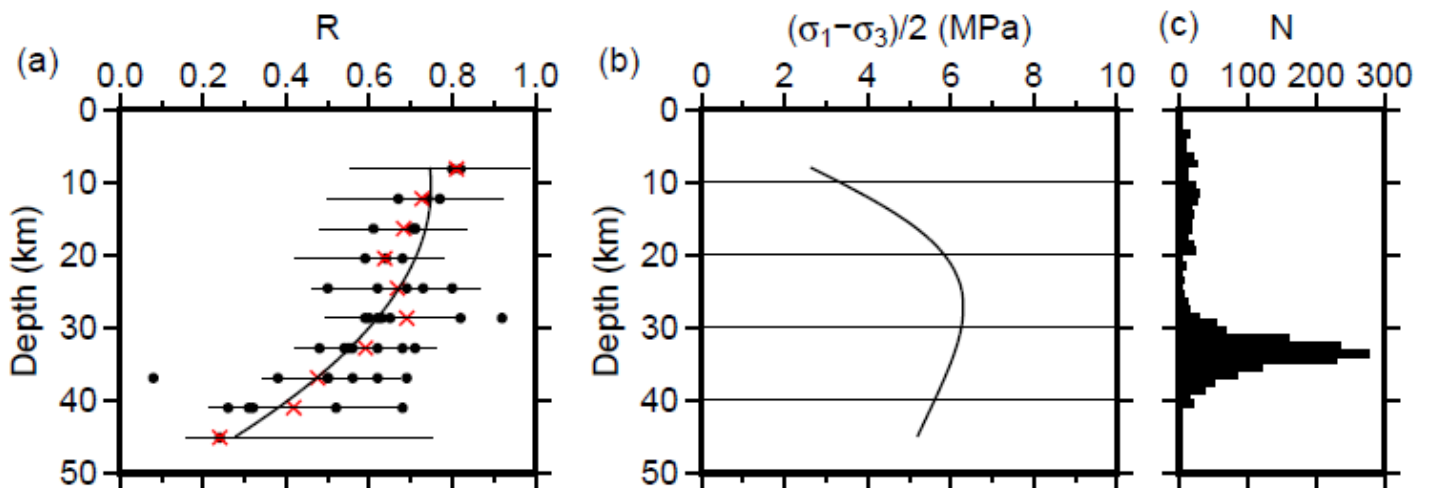


Figure 10

Depth dependency of the stress ratio R . (a) black dots are the R -value at each node and red crosses are the averaged values at each depth. Horizontal thin lines indicate the estimation error. A curved line is the

best fitted line to the red crosses. (b) the maximum shear stress $\tau_{\max} = (\sigma_1 - \sigma_3) / 2$ as a function of depth. (c) Histogram of the depth of aftershocks shown in Fig. 3.

Supplementary Files

This is a list of supplementary files associated with this preprint. Click to download.

- [fig00.pdf](#)
- [3StressList.csv](#)
- [2MecanismsList.csv](#)
- [1StationList.csv](#)